PA200 differentially regulates the proteasome and inhibits migration of cancer cells

Ayse Seda Yazgili[1*], Georgia A. Giotopoulou[1], Sabine J. Behrend[1], Frauke Koops[2,3], Vanessa Welk[1], Thomas Meul[1], Linda Zemke[2], Norbert Reiling[2], Torsten Goldmann[2,3], Georgios T. Stathopoulos[1,4], Silke Meiners[1,2,3,5]

[1]Comprehensive Pneumology Center (CPC), University Hospital of the Ludwig-Maximilians-University (LMU) and Helmholtz Center Munich, Member of the German Center for Lung Research (DZL), Max-Lebsche Platz 31, 81377, Munich, Germany

[2]Research Center Borstel/Leibniz Lung Center, 23845, Borstel, Germany

[3]Airway Research Center North (ARCN), Member of the German Center for Lung Research (DZL)

[4]Medical School, University of Cyprus, 2029 Aglantzia, Nicosia, Cyprus

[5]Institute of Experimental Medicine, Christian-Albrechts University, Kiel, Germany

**Present Address: The CRUK Scotland Institute, Garscube Estate, Switchback Road, Bearsden, Glasgow, G61 1BD, United Kingdom*

Correspondence to:

Prof. Silke Meiners, PhD, Research Center Borstel/Leibniz Lung Center, Parkallee 1-40, 23845 Borstel, Germany, Phone +49 (0)4537 188 -5846, Email: smeiners@fz-borstel.de

Competing Interests

The authors declare no competing financial interests.

Running title:

PA200 in lung cancer

ABSTRACT

Proteasome activator 200 (PA200) is upregulated in non-small cell lung cancer (NSCLC) and linked to poor prognosis. We previously demonstrated that the overexpression of PA200 in NSCLC is associated with immune evasion and reduced responsiveness to immune checkpoint inhibitors. The cell autonomous function of PA200 in cancer growth, however, is not solved.

We here demonstrate that deletion of PA200 in two distinct lung cancer cell lines induced cell-specific alterations in proteasome composition and activities with a minor direct impact on overall proteasome activity. Deficiency of PA200 in lung cancer cells did not consistently alter tumor cell growth *in vitro* and *in vivo*. However, we observed concerted inhibition of tumor cell migration and invasion with conserved downregulation of the integrin ITGB3 and transcriptional dysregulation of multiple cell adhesion and ECM regulators. Our transcriptome profiling revealed a striking disparity in the transcriptional response to PA200 deletion in the two lung cancer cell lines. Together with our PA200 interactome analysis that uncovered an unexpected cell-dependent profile of PA200-interacting proteins, our data indicate that the function of PA200 is cell-specific and depends on the cellular context. In conclusion, we here demonstrate that PA200 cell-autonomously regulates the invasive capacities of tumor cells thereby potentially promoting lung cancer spread and metastasis formation. This mechanism might add to PA200-related immune evasion and may contribute to the observed poor prognosis of PA200-overexpressing lung cancer patients.

45 **INTRODUCTION**

46 The proteasome system is key for regulated intracellular protein degradation. It consists of
47 multiple proteasome complexes that share a common proteolytic core, the 20S
48 proteasome, but differ in their associated proteasome activators which fine-tune substrate
49 degradation by the proteasome [1]. The 20S proteasome contains three active sites that
50 cleave the proteins after hydrophobic, basic, and acidic amino acids constituting the
51 chymotrypsin-like, trypsin-like and caspase-like proteolytic activities, respectively [2]. These
52 active sites can be exchanged by inducible subunits, i.e. LMP7, MECL1, and LMP2 to
53 assemble into the immunoproteasome that has altered proteolytic activities [3]. The
54 proteasome activators modulate proteasome function in specific cellular compartments and
55 in an ATP- and ubiquitin-dependent or -independent manner [1]. The well-known 19S
56 regulator binds to the 20S proteolytic core either on one or both ends forming the 26S and
57 30S proteasome, respectively. These proteasome complexes mediate ATP- and ubiquitin-
58 dependent protein degradation [4]. Yet, alternative proteasome activators including PA28αβ,
59 PA28γ, and PA200 act ATP- and ubiquitin-independently and have distinct subcellular
60 functions [2].

61 PA200, encoded by the PSME4 gene, is expressed at low levels in most cells of the organism
62 except for germ line cells [5]. PA200 has been implicated in various cellular processes, such as
63 DNA damage repair [6,7], mitochondrial and proteostasis stress responses [8,9], myofibroblast
64 differentiation [10], aging [11,12], and protection from neuropathy [13,14]. It is upregulated in lung
65 fibrosis, melanoma and lung cancer [10,15,16]. PA200 was recently shown to restrict antigenic
66 diversity of non-small cell lung cancers (NSCLC) favoring immune evasion and
67 responsiveness to immune checkpoint inhibition [15]. The cell-autonomous role of PA200 in
68 cancer, however, remains elusive.

69 In this study, we investigated the functional role of PA200 in lung cancer by genetically
70 deleting PA200. We used two distinct lung cancer cell lines, A549 and H1299, and
71 characterized them thoroughly regarding proteasome regulation, cellular growth and
72 migration capacity. Our findings revealed a striking disparity of PA200 deficiency on
73 proteasome complex regulation and transcriptional profile for the two cancer cell lines,
74 however cancer cell growth was not consistently altered by PA200 knockout. In contrast, we
75 found that PA200 deletion resulted in decreased cell migration and extracellular matrix
76 (ECM) interactions consistently in both cell lines. Our data suggests that PA200 plays a cell-
77 autonomous role in the invasive capabilities of tumor cells, which may contribute to the
78 spread of lung cancer and the formation of metastases. This mechanism might add to
79 PA200-related immune evasion and may contribute to the observed poor prognosis of
80 PA200-overexpressing lung cancer patients [15].
81
82 **RESULTS**
83 **Deletion of PA200 in lung cancer cell lines differentially impacts proteasome function and**
84 **assembly**
85 We first confirmed the oncogenic role of PA200 in lung cancer by analysis of PA200 protein
86 expression in different lung cancer types, i.e., lung adenocarcinoma (LUAD), squamous cell
87 carcinoma (SQCLC), and small cell lung cancer (SCLC), in a cohort of 60 patients using
88 immunohistochemistry with a validated antibody [10,17]. Expression of PA200 is generally low
89 in lung parenchymal and immune cells, as previously demonstrated by us [10]. We observed
90 significantly increased expression of PA200 in LUAD and SQCLC compared to SCLC tumors
91 (Suppl. Figures S1A-B). PA200 was also strongly upregulated in a genetic model of Kras-

92 induced lung adenocarcinoma in mice (Suppl. Figure S1C) supporting its induction upon
93 oncogenic transformation of epithelial cells [18].
94 To elucidate the functional role of PA200 in cancer, we deleted PA200 in two lung cancer
95 cell lines, i.e. A549 and NCI-H1299 (hereinafter H1299) using CRISPR/Cas9 technology.
96 Complete loss of PA200 was confirmed for several A549 and H1299 cell clones by RT-qPCR
97 (Figure 1A), Western blotting (Figures 1B-C) and DNA sequencing (Suppl. Figure S1D). We
98 noted that H1299 cells express more PA200 than A549 cells, as observed for mRNA (Figure
99 1A) and protein levels (Figure 1B). Unexpectedly, deletion of PA200 in the two cell lines
100 affected proteasome activity differentially: In A549 cells, both the total chymotrypsin-like
101 (CT-L) and total caspase-like (C-L) activities were significantly reduced compared to WT
102 controls (Figure 1D), while H1299 PA200 knockout (KO) cells displayed significant activation
103 of these two activities (Figure 1E). Contrary to previous findings [15,19], loss of PA200 did not
104 affect the total trypsin-like (T-L) activity (Figures 1D-E). To analyze these cell-specific effects
105 of PA200 on the proteasome in more detail, we performed native gel analysis to determine
106 the activity, composition, and abundance of distinct proteasome complexes [20]. In A549
107 PA200 KO cells, the CT-L activity of the 20S was slightly activated while the activity of 26S
108 and 30S complexes were not significantly altered (Figure 2A). In H1299 PA200-deficient
109 clones, 20S activity was reduced while 30S activity was elevated (Figure 2B). Blotting of the
110 native gel and probing for the α-20S subunits (α1-7), revealed no significant changes in the
111 abundance of the proteasome complexes upon PA200 deletion in A549 cells (Figure 2A) but
112 elevated abundance of 30S proteasome complexes in H1299 PA200 knockout clones
113 accounting for their elevated 30S activity (Figure 2B). Of note, we observed a strikingly
114 divergent composition of proteasome complexes upon deletion of PA200 (Figures 2A-B).
115 PA200-deleted A549 clones assembled higher levels of immunoproteasome subunits in the

116 20S (for LMP7) and 26S and 30S complexes (for MECL1 and LMP2) and had higher levels of
117 PA28 activator bound to the 20S (Figure 2A). The increased assembly of the
118 immunoproteasome could explain the reduced C-L activity in PA200-deleted A549 clones
119 (Figure 1C). In contrast, incorporation of the immunoproteasome subunits was significantly
120 decreased in PA200-deleted H1299 cells (Figure 2B). The levels of PA28α and PA28β were
121 not significantly regulated in H1299 (Figure 2B), however PA28β was upregulated
122 significantly in A549 PA200 KO cells (Figure 2A). Our results suggest that the deletion of
123 PA200 has a minor direct impact on overall proteasome activity but rather contributes to
124 cell-specific adjustment of proteasome composition and activities.
125
126 **PA200 deficiency does not alter tumor cell growth *in vitro* and *in vivo***
127 We next aimed to investigate the cellular consequences of PA200 deletion and differential
128 proteasome regulation and investigated the growth of the lung cancer cell lines. In A549
129 cells, deletion of PA200 slightly reduced proliferation rates (Figure 3A) but did not affect
130 colony formation (Figure 3B). H1299 cells did not show any significant alteration neither in
131 proliferation (Figure 3A) nor in colony formation assays (Figure 3B). To analyze tumor cell
132 growth *in vivo*, we injected pools of A549 and H1299 PA200 WT and KO cell clones into the
133 flanks of immunocompromised SCID mice and monitored tumor growth and body weight for
134 8 weeks. SCID mice are deficient in B and T cells and therefore lack adaptive immune
135 responses. This model thus allows us to dissect the cell-autonomous function of PA200 in
136 tumor growth in the absence of its immune-modulating function [15]. The development of
137 primary tumors was reduced for A549 PA200 KO cells (Suppl. Figure S2A) while all animals
138 with H1299 WT and PA200 KO cells injected developed tumors. For both cell lines, we
139 observed delayed flank tumor development of PA200 deleted cells. Tumor growth rates,

140 however, normalized over 60 days and were not significantly different from respective WT
141 controls at the endpoint of analysis (Figures 3C-D, Suppl. Figures S2B-E). Ki-67 staining of
142 primary tumors did not reveal any significant difference in the number of proliferating cells
143 between the WT and PA200-deleted tumors (Figures 3E-F). These *in vitro* and *in vivo* data
144 demonstrate that PA200 does not consistently alter tumor cell growth in a cell autonomous
145 manner.
146
147 **PA200 deficiency inhibits tumor cell migration and invasion capacity *in vitro***
148 We further characterized the effects of PA200 deletion with regard to another hallmark of
149 cancers, i.e. their capacity to migrate and invade the extracellular matrix (ECM) [21] and
150 analyzed the effect of PA200 deletion in wound healing and migration assays. Loss of PA200
151 in A549 cells reduced invasion of matrigel-embedded A549 spheroids (Figure 4A). As H1299
152 cells are unable to form spheroids, we assessed their migration efficiency in a Boyden
153 chamber assay and showed prominent loss of migration capacity upon PA200 deletion
154 (Figure 4B). Using a standardized wound-healing assay, we confirmed reduced migration
155 and wound closure of both A549 and H1299 PA200 KO cells (Figures 4C-D). We next
156 assessed whether deletion of PA200 promotes epithelial-mesenchymal transition (EMT), a
157 hallmark feature of invasive epithelial tumor cells [21]. Upon KO of PA200, the epithelial
158 adherens junction protein E-cadherin but also the mesenchymal N-Cadherin were
159 significantly upregulated on the protein level in both A549 and H1299 cells (Figure 4E).
160 Expression of the tight junction component claudin and the mesenchymal markers, such as
161 vimentin and β-catenin, was not regulated by PA200 deficiency (Figure 4E). Deletion of
162 PA200, however, induced strong and concerted downregulation of Integrin-β3 (ITGB3)
163 expression on RNA and protein levels in both lung cancer cell lines (Figure 4E and Suppl.

164 Figures S3A-B). Taken together, our results indicate that PA200 plays a conserved role in the
165 regulation of cell migration and invasion of lung cancer cells, potentially related to
166 downregulation of ITGB3.
167
168 **Transcriptomic analysis highlights conserved downregulation of ECM-related genes in**
169 **PA200-deficient lung cancer cells**
170 To disentangle cell-specific from conserved effects of PA200 deletion, we performed
171 transcriptional profiling of our WT and PA200 KO A549 and H1299 cell clones. The
172 transcriptomes of WT and KO clones were clearly distinct as highlighted by PCA analysis
173 (Suppl. Figures S4A-B). Deletion of PA200 had a more substantial transcriptional effect in
174 A549 compared to H1299 cells with 345 genes being down- and 419 up-regulated in PA200-
175 deleted A549 cells and 288 genes down- and 196 genes up-regulated in H1299 PA200 KO
176 clones (Figures 5A-C). Surprisingly, we found only 16 genes that were co-regulated both in
177 PA200-deleted A549 and H1299 clones (highlighted in red (up) and blue (down)). These
178 included, besides PSME4, several proteins involved in cytoskeletal organization, cell
179 adhesion and remodeling, and interaction with ECM. Amongst them, we confirmed ITGB3 as
180 concertedly downregulated in both lung cancer cell lines (Figure 5C). Reactome pathway
181 and molecular signature database (MsigDB) analysis of differentially regulated genes
182 confirmed that PA200 deletion in both A549 and H1299 cell lines, concertedly regulated
183 pathways related to ECM formation such as collagen formation, ECM organization,
184 proteoglycans, and integrin and surface organization-related genes (Figures 5D-G, Suppl.
185 Figure 4C-D). Our transcriptional analysis thus confirms a conserved role for PA200 in the
186 regulation of invasion and migration that is mediated by transcriptional regulation of cell
187 adhesion and ECM regulators. At the same time, the minimal overlap of the transcriptional

188 response to PA200 deletion in the two NSCLC cell lines indicates that the function of PA200
189 is cell-specific and depends on the cellular context.
190
191 **Pulldown of PA200 reveals differential interactome in lung cancer cell lines**
192 These prominent cell-specific effects of PA200 deletion led us to assume that PA200 has
193 differential roles in the two cancer cell lines that might be revealed by its interactome. To
194 determine PA200 interactors, we immunoprecipitated PA200 from A549 and H1299 WT cell
195 lines. Interacting proteins were identified by mass-spectrometry. Immunoprecipitation of
196 PA200 from the respective PA200 KO clones was used as a specificity control (Figure 6A).
197 Our interactome analysis of PA200 identified 91 (A549) and 41 (H1299) interacting proteins
198 with only a minimal overlap of three proteins including PA200 (PSME4) (Figure 6B). We were
199 surprised not to detect any significant enrichment of proteasomal subunits in our mass-
200 spectrometry data, even though 20S subunits were clearly enriched in the PA200 pulldowns
201 (Figure 6A). This might be due to the weak unspecific binding of the proteasome to the anti-
202 PA200 antibody (Figure 6A) which could explain why proteasome subunits were not
203 detected as significantly enriched when we compared interacting proteins between WT and
204 respective KO clones. In the next step, we analyzed our interacting proteins with MSigDB
205 and Reactome databases to understand the functions and pathways of the PA200
206 interactors. In A549 cells, the interactors of PA200 were mainly related to E2F and Myc
207 targets, reactive oxygen species, ultraviolet (UV) response, glycolysis, and G2-M checkpoint
208 proteins (Figures 6C and 6E). Reactome pathway analysis showed that the PA200 interactors
209 in A549 cells were mainly involved in DNA processes (Suppl. Figure S5A). PA200 interacting
210 proteins in H1299 cells were related to the molecular signatures of the mitotic spindle, UV
211 response, mTORC1 and PI3K/AKT/mTOR signaling (Figures 6D and 6F). In the Reactome

212 analysis, they showed enrichment in Rho GTPase signaling and regulation of transcription
213 (Suppl. Figure S5B). Concludingly, these data reveal an unexpected cell-specific profile of
214 PA200 interacting proteins which might explain the differential cellular response to PA200
215 deletion in A549 and H1299 lung cancer cell lines.
216
217 **DISCUSSION**
218 We here uncover adaptive cellular responses to PA200 deletion that depend on the cellular
219 context and are cell line specific. In our comprehensive analysis of two different lung cancer
220 cell lines, we discovered an almost entirely distinct interactome of PA200 which coincided
221 with differential cellular and transcriptional responses to genetic deletion of PA200. PA200
222 deficiency had cell-specific effects on the proteasome complex system resulting in distinct
223 alterations in proteasome complex composition and activity. Among the conserved
224 responses to PA200 deletion in the two cancer cell lines, we discovered cell-autonomous
225 downregulation of cell migration and invasion upon transcriptional alterations in cell-
226 adhesion and ECM-related genes such as ITGB3.
227 Deleting PA200 altered the activity and composition of proteasome complexes but with
228 opposite outcomes depending on the cell line: While total CT-L and C-L activities were
229 decreased in A549 cells, they were increased in H1299 cells upon PA200 deletion.
230 Furthermore, in-gel proteasome activity assays revealed a shift in proteasome complex
231 activities and composition including differential assembly of immunoproteasomes and
232 association of PA28 regulators. These data reveal cell-specific adaptive remodeling of the
233 proteasome system in response to PA200 deficiency. Our data are in line with previous
234 findings from our own lab on the adaptation of the proteasome system upon transient
235 knockdown of PA200 in primary human lung fibroblasts [10]. Similarly, VerPlank et al. recently

236 demonstrated that proteasomal degradation was activated in PA200 KO animals,
237 contributing to protection from proteotoxic neuropathy [13]. The differences between the two
238 cell lines were not limited to proteasome activities but proteasome remodeling was
239 associated with a differential transcriptional response. For example, inflammatory signaling
240 was a prominent feature of PA200 KO in A549 cells, while this pathway was downregulated
241 in H1299 PA200 KO cells. This discrepancy might explain the increased assembly of the
242 immunoproteasome in A549 KO cells. Moreover, we noted that the interactome of PA200
243 between the two cell lines is very different with only two overlapping proteins. This might
244 relate to weak and transient interactions that were stabilized upon pulldown of PA200 using
245 a mild and non-stringent immunoprecipitation protocol or due to different subcellular
246 localization and functional annotation of PA200-containing proteasome complexes. The
247 latter is supported by the differential interaction of PA200 with the DNA and replication
248 machinery in A549 cells versus transcription- and GTPase-related interactions in H1299 cells.
249 One could also speculate that the divergent cell-type specific effects relate to the role of
250 PA200 in DNA repair and histone degradation [6,7,22,23]. This observation aligns with the
251 finding that inositol-6-phosphate (IP6), a nuclear regulator of enzyme function and DNA
252 repair [24], is an integral component of PA200 as evidenced by structural analyses (Toste Rêgo
253 and da Fonseca 2019; Guan et al. 2020). Furthermore, the mutational background (A549
254 with KRAS activating mutation, H1299 loss of TP53), the origin (A549 primary lung
255 adenocarcinoma [26] and H1299 metastatic lymph node [27] and the different baseline PA200
256 expression levels of the two cell lines could explain the observed functional differences. Our
257 data thus indicate that the effects of PA200 need to be carefully analyzed depending on the
258 cellular background.

259 In the lung cancer cells, we did not observe any consistent effects of PA200 deficiency on
260 tumor cell growth, neither *in vitro* nor *in vivo*. These data are supported by our
261 transcriptome analysis where we did not find any prominent regulation of growth related
262 pathways upon deletion of PA200 in A549 and H1299 cells. Our data also accord with
263 observations from PA200 KO mice that did not form tumors even when crossed to p53
264 mutant mice [5]. While transient knockdown of PA200 in Hela cells increased cell growth in
265 the presence of glutamine in a previous study [28], however PA200-deleted A549 and H1299
266 clones showed different glutamine-sensitivity (data not shown). While cell growth was
267 unaffected, PA200 deficiency impaired migration and invasiveness of lung cancer cells. This
268 effect was conserved in both lung cancer cell lines and corroborated using several
269 complementary functional assays such as wound healing, Boyden chamber and Matrigel
270 invasion assays. This decrease in the invasive capacity in PA200 deficient cancer cells can be
271 explained by transcriptomic regulation of several cell-adhesion and ECM regulators.
272 Although, there were very few genes that were concertedly regulated by PA200 deletion in
273 A549 and H1299 cells, the overall transcriptomic response to PA200 deletion was similar
274 with integrin cell surface interactions and non-integrin membrane interactions being
275 downregulated. A prominent and concertedly reduced cell-matrix adhesion molecule was
276 integrin beta 3 (ITGB3), a well-established driver of metastasis in several solid cancer types
277 and associates with poor prognosis [29–32]. We confirmed its downregulation by qRT-PCR and
278 Western blot analysis. However, aAs our MS-based PA200 interactome analysis did not show
279 ITGB3 as a direct PA200 interactor, dysregulation of ITGB3 might be indirect.
280 Taken together, our data, together with the results of the Merbl lab [15], point towards a
281 tumor-promoting role of PA200 in lung cancer related to its ability to regulate cell migration,
282 invasion, and immunogenicity.

283

284 **MATERIALS AND METHODS**

285 **Cell culture and generation of knockout cell lines**

286 The human lung cell lines were obtained from DSMZ or were a gift from Dr. Georgios
287 Stathopoulos. The cell lines were cultured at 37˚C and 5% CO_2 in a humidified incubator.
288 A549 cells (RRID:CVCL_0023) were grown in DMEM/F12 medium, while NCI-H1299 cells
289 (RRID:CVCL_0060) were cultured in RPMI-1640 medium, both supplemented with 10% FBS
290 and 100 U/mL penicillin/streptomycin.

291 Low passage number cells were harvested at 80% confluency. Transfection of TrueCut Cas9
292 Protein v2, Hs.Cas9.PSME4.1.AB and tracRNA (IDT, Leuwen, Belgium) was performed using
293 the Lipofectamine CRISPRMAX Transfection Reagent protocol (Thermo Fisher Scientific). The
294 cells were incubated at 37°C for 48 h after transfection. Following the incubation period, the
295 cells were collected, and 50 cells were seeded onto 15 cm dishes. After 2 weeks, colonies
296 were picked with trypsin-incubated cloning disks and transferred to 24-well (one colony per
297 well). To confirm the knockout efficiency, protein and DNA were isolated. For PCR-based
298 amplification we used forward primer 5´ATCTGCAAGAGAGATGCAGCC 3´ and reverse primer
299 5´AGGTTTGAGCAGCAGCAAGA 3´. For Sanger sequencing reverse primer
300 5´TGGATGGGGAAAGCAAAACCC 3´ was used.

301 **Cell proliferation and colony formation assays**

302 The proliferation rate of different cell types was assessed using established methodology
303 [33,34]. A549 (30 000 cells/well) and NCI-H1299 (40 000 cells/well) cells were seeded into 6-
304 well plates. The initial cell count was determined on day 1, and the final cell count was
305 recorded on day 4 to calculate the rate of cell division per day according to the proliferation
306 Rate formula = $\log_2$ [(Final day cell count (Day 4) / Initial day cell count (Day 1))] / (Final day -

307 Initial day (3 days)). A colony formation assay was conducted by seeding 100 NCI-H1299 and
308 200 A549 cells in 6-well plates as previously described [35]. The culture medium was refreshed
309 on day 3 and day 7. On day 10, the cells were fixed using 4% formaldehyde, stained with 1%
310 crystal violet dye (Sigma), photographed, and quantified.

311 **Migration and invasion assays**

312 For Boyden chamber migration analysis, a 10% FBS medium was used as a chemoattractant
313 in 24-well plates. Boyden chambers (Biotrend, Cologne, Germany) containing 100 000 NCI-
314 H1299 cells in 0% FBS medium were inserted into the wells. After 24 hours, the cells were
315 fixed with 4% formaldehyde and stained with 1% crystal violet solution. Excess dye was
316 washed off, and the chambers were left to dry before imaging with Axio Observer.Z1/7
317 (Zeiss, Oberkochen, Germany).

318 For wound healing assays, inserts (Ibidi, Graefelfing, Germany) were used to assess cellular
319 wound healing capacity. The inserts were placed into a 24-well plate (1 insert/well), with
320 A549 (28 000 cells/insert side) and NCI-H1299 (20 000 cells/insert side) cells seeded on both
321 sides. Inserts were removed after 24 h and 1 ml of medium was added. For experiments
322 related to Figure 4, H1299 cells were incubated in a live cell imaging microscope (Axio
323 Observer.Z1/7, Zeiss) at 37°C and 5% CO_2 for 48 h or until the 500 µm gap closed. Images
324 from different time points were calculated using the Wound Healing Tool macro on ImageJ
325 (RRID:SCR_003070) [36]. A549 cells were imaged in a live cell imaging multimode reader
326 (Cytation1, Agilent Technologies, Waldbronn, Germany) at 37°C and 5% CO_2 for 48 h. Using
327 a 4x objective, one to two images per well were captured at different time points using
328 bright field imaging channels. If two pictures were taken, the images were stitched prior to
329 analysis. Images were analyzed using the Gen5 3.16 Software (Agilent Technologies)
330 following the application note "Incorporation of a Novel, Automated Scratch Tool and

331 Kinetic Label-Free Imaging to Perform Wound Healing Assays" by Brad Larson (Agilent
332 Technologies).
333 For gel invasion assays, a total of 5 000 A549 cells were seeded in low attachment U-bottom
334 96-well plates (Neolab, Heidelberg, Germany) with 100 µl of medium and centrifuged briefly
335 for 2 minutes at 1 000 rpm to establish initial cell-cell contact. The cells were then incubated
336 for 72 h under standard conditions. After this incubation period, the spheroids were gently
337 collected into 1.5 ml Eppendorf tubes and allowed to settle on the tube's bottom for 5 min
338 on ice. Subsequently, a collagen G matrix gel was prepared, as described previously [37].
339 Briefly, solution A was created by combining 1 M HEPES buffer (pH= 7-7.5) and 0.7 M NaOH
340 in equal proportions. Solution A was mixed with 20% FBS in 10× PBS (pH = 7.4) in a 1:1 ratio
341 to create solution B (pH = 7.90–8.05). For the final gelation step, collagen G and solution B
342 were mixed in a 4:1 ratio (v:v). To create a collagen G+Matrigel matrix, a mixture of collagen
343 G matrix gel and Matrigel was prepared in a 1:1 ratio (v:v). The spheroids were transferred
344 into the matrix mixture and placed in an incubator to solidify over a period of 5 h. After
345 solidification, the spheroids were imaged using a live cell imaging microscope for 72 h.
346 **Western Blot analysis**
347 Denatured protein extracts were generated with the RIPA lysis buffer (50 mM Tris/HCl pH
348 7.5, 50 mM NaCl, 1% IGEPAL, 0.5% Sodium deoxycholate, 0.1% SDS). Briefly, frozen cell
349 pellets were dissolved in RIPA buffer supplemented with protease inhibitor (Roche
350 Diagnostics, Mannheim, Germany) and phosphatase inhibitor (Roche Diagnostics). The cell
351 lysis process was carried out on ice and lasted for 20 minutes, with periodic vortexing during
352 this period. Subsequently, the lysates were centrifuged at 15 000 rpm and 4°C for 20
353 minutes to remove cellular debris. Protein concentrations were calculated with BCA assay
354 according to manufacturer's recommendation (Pierce BCA Protein Assay Kit, Thermo Fisher

355 Scientific) and 15 µg protein extracts were diluted with Milli-Q® water and mixed with 6x
356 Laemmli buffer to a final concentration of 1x. Samples were denatured at 95 °C for 15 min.
357 Polyacrylamide gels were prepared and cast using Bio-Rad equipment (Bio-Rad, Munich,
358 Germany). Denatured protein extracts were loaded on the gel and electrophoresis was
359 performed at 90 - 120 V.
360 Proteins were transferred to a methanol-activated PVDF membrane at 250 mA for 90 min at
361 4°C. Membranes were blocked with Roti®-Block (1 h) or EveryBlot (10 min). Primary
362 antibodies were incubated overnight at 4°C, followed by three 15-minute PBST washes.
363 HRP-conjugated secondary antibodies were applied for 1 hour at room temperature. After
364 two PBST washes, chemiluminescence was detected using Luminata™ or SuperSignal
365 reagents with iBright CL1500 (Thermo Fisher Scientific) or ChemiDoc (Bio-rad) systems.
366 Densitometric analysis was conducted using ImageLab software.
367 **Table 1: List of antibodies (Rb: Rabbit, Ms: Mouse, Gt: Goat, mAb: Monoclonal, pAb:**
368 **Polyclonal)**

Target	**Catalog Number**	**Host & Type**	**Research Resource Identifier (RRID)**	**Company**
Claudin-1 (D5H1D)	13255	Rb mAb	AB_2798163	Cell Signaling Technology (Leiden, Netherlands)
E-Cadherin (24E10)	3195	Rb mAb	AB_2291471	Cell Signaling Technology
Integrin β3 (ITGB3)	D7X3P	Rb mAb	Not listed	Cell Signaling Technology

N-Cadherin (D4R1H)	13116	Rb mAb	AB_2687616	Cell Signaling Technology
PA200	NBP1-22236	Rb pAb	Not listed	Novus Biologicals (Bio-Techne, Wiesbaden, Germany)
Vimentin (D21H3)	5741	Rb mAb	AB_10695459	Cell Signaling Technology
α1-7 (MCP231)	ab22674	Ms mAb	AB_2171376	Abcam (Amsterdam, Netherlands)
β-Actin (HRP-linked)	A3854	Ms mAb	AB_262011	Sigma-Aldrich (Darmstadt, Germany)
β-Catenin (D10A8)	8480	Rb mAb	AB_11127855	Cell Signaling Technology
Lmp2 (Psmb8)	ab3328	Rb pAb	AB_303707	Abcam
Lmp7 (Psmb9)	ab3329	Rb pAb	AB_303708	Abcam
MECL-1 (Psmb10)	ab190790	Rb mAb	Not listed	Abcam
Pa28α	ab155091	Rb mAb	AB_2801483	Abcam
Pa28β	sc-23642	Gt pAb	AB_2171080	Santa Cruz (Heidelberg, Germany)
Anti-goat IgG HRP-linked	61-1620	Rb	AB_2533922	Thermo Fisher Scientific
Anti-mouse IgG HRP-linked	7076	Hs	AB_330924	Cell Signaling Technology

Anti-rabbit IgG HRP-linked	7074	Hs	AB_2099233	Cell Signaling Technology

369

370 **PA200 interactome analysis**

371 For immunoprecipitation of PA200, cells were lysed in TSDG buffer (10 mM Tris pH 7.0, 10
372 mM NaCl, 1.1 mM $MgCl_2$, 0.1 mM EDTA, 1 mM DTT, 1mM NaN_3, 10 % (v/v) Glycerol) under
373 native conditions as described previously to preserve physiological protein-protein
374 interactions [10,20]. Pre-clearing of the lysates was performed using magnetic Dynabeads
375 coated with Protein A for antibodies raised in rabbits (Thermo Fisher Scientific) on a
376 magnetic rack. 20 µL of Dynabeads were transferred to protein LoBind tubes (Eppendorf)
377 and washed twice with 500 µL phosphate buffer pH 7.4. 200 µg protein lysate (in TSDG
378 buffer + 0.2 % IGEPAL) was incubated with the Dynabeads for 20 minutes at room
379 temperature on a rotator (20 rpm) in a pre-clearing step which allows the saturation of the
380 unspecific binding sites of the Dynabeads with proteins from the cell extracts and thereby
381 reduces unspecific background binding. In the meantime, 30 µl Dynabeads were washed
382 twice with 100 µL phosphate buffer pH 7.4. Beads were resuspended in 50 µL phosphate
383 buffer pH 7.4 and incubated with 3 µL of the anti-PA200 antibody (NBP1-22236, Novus) for
384 15 minutes at 1250 rpm and room temperature. Afterwards, beads were washed twice with
385 100 µL TSDG buffer + 0.2 % IGEPAL. 50 µl of the TSDG buffer + 0.2 % IGEPAL was used to
386 resuspend the beads-antibody complexes. Precleared 200 µg TSDG protein lysates
387 (separated from the beads) were added onto the beads bound to the antibody to a total
388 volume of 250 µl. Samples were incubated with a rotator (20 rpm) for 2 hours at 4 °C. 25 µL
389 per sample of the total mixture was used as input. 25 µl supernatant was collected once the
390 beads had been separated on the magnetic rack. Input and supernatant samples (25 µl) were

391 mixed with 6x loading buffer (5 µl) and heated at 95 °C for 10 min. Beads were washed five
392 times (pre-cleared) with 500 µL TSDG buffer supplemented with 0.2 % IGEPAL and one final time
393 with TSDG buffer. Co-immunoprecipitated proteins were eluted in 25 µL 1x Laemmli buffer and
394 further denatured for 10 min at 95 °C. Eluted proteins were further analyzed by Western
395 blotting together with the input and supernatant samples or sent to the Research Unit Protein
396 Science (HMGU) for mass spectrometry analysis.

397 **In-gel proteasome activity assay**

398 Native gel electrophoresis was performed to analyze intact and active proteasome
399 complexes, following previously optimized and detailed protocol [20]. Briefly, frozen cell
400 pellets were thawed and lysed in OK lysis buffer (50 mM Tris/HCl pH 7.5, 2 mM DTT, 5 mM
401 MgCl2, 10% glycerol, 2 mM ATP, 0.05% digitonin) supplemented with protease and
402 phosphatase inhibitors (Roche Diagnostics). Cells were lysed on ice for 20 min with
403 intermittent vortexing, followed by centrifugation at 15 000 rpm for 20 min at 4°C. Protein
404 concentration was determined by BCA assay, and 15 µg of protein was diluted with water,
405 mixed with 5x native gel loading buffer, and loaded onto 3-8% gradient NuPAGE Novex Tris-
406 acetate gels (Themo Fisher Scientific). Electrophoresis was performed at 150 V for 4 h at 4°C
407 in native gel running buffer. Following electrophoresis, an in-gel proteasome activity assay
408 was conducted to assess chymotrypsin-like (CT-L) activity using an activity buffer (50 mM
409 Tris, 1 mM ATP, 10 mM $MgCl_2$, 1 mM DTT, and 0.05 mM Suc-LLVY-AMC). Fluorescence was
410 detected using the ChemiDoc XRS+ system (Bio-Rad). For immunoblotting, gels were
411 incubated in solubilization buffer (2% SDS, 66 mM Na_2CO_3, 1.5% β-mEtOH) for 15 min before
412 protein transfer.

413 **Total proteasome activity assay**

414 The activity of the 20S proteasome's active sites—chymotrypsin-like (CT-L), caspase-like (C-
415 L), and trypsin-like (T-L)—was evaluated using the Proteasome-Glo™ Assays (Promega,
416 Fitchburg, Wisconsin, USA), following the manufacturer's instructions. In brief, 1 µg of
417 protein from OK lysates was mixed with OK lysis buffer (see above) to ensure equal
418 volumes, and the final volume was adjusted to 20 µL with water. These dilutions were
419 transferred to white flat-bottom 96-well plates and combined with 20 µL of the specific
420 substrates. Luminescence was measured at 2-min intervals over 45 min using a Tristar LB
421 941 plate reader (Berthold Technologies, Bad Wilsbad, Germany). Each sample was analyzed
422 in quadruplicate, and the plateau values of the luminescent signal were used for quantifying
423 proteasome activity for each specific substrate.

424 **RNA isolation**

425 For RT-qPCR, cellular RNA was isolated using the Roti®-Quick Kit (Roth, Karlsruhe, Germany)
426 via phenol-chloroform extraction according to manufacturer's instructions. Briefly, cells
427 were lysed in Quick 1 solution, followed by the addition of Quick 2 solution. Samples were
428 incubated on ice for 10 minutes, then centrifuged at 10 000 rpm and 4°C for 15 min to
429 separate phases. The upper aqueous phase was carefully collected and transferred to a new
430 tube and Quick 3 solution was added. The samples were incubated either at -80°C for 40
431 min or at -20°C overnight. RNA was pelleted by centrifugation at 13 000 rpm and 4°C for 20
432 min, followed by washing twice with 70% ethanol. The RNA pellet was air-dried on ice and
433 reconstituted in 25-40 µL of nuclease-free water

434 For bulk RNA sequencing, RNA was isolated using an RNA isolation kit (VWR, Darmstadt,
435 Germany) according to the provided protocol. Cell pellets were lysed in TRK buffer with 2%
436 β-mEtOH and homogenized using a peqGOLD RNA Homogenizer Column (VWR). Following
437 centrifugation at ≥12 000 x g for 2 min, the flow-through was mixed with ethanol (70%) and

438 vortexed. The mixture was then passed through a peqGOLD RNA Mini Column via
439 centrifugation at 10 000 x g for 1 min. The column was washed with RNA Wash Buffer I and
440 80% ethanol, followed by centrifugation steps to remove residual ethanol. RNA was eluted
441 by nuclease-free water and concentration was determined using the NanoDrop 1000
442 (Thermo Fisher Scientific).

443 **Reverse transcription of RNA and RT-qPCR**

444 For the reverse transcription process, RNA ranging from 0.25 to 1 µg was mixed with 9 µL
445 of nuclease-free water, followed by the addition of 2 µL of 250 µM Random Hexamers
446 (Thermo Fisher Scientific). After allowing the mixture to incubate at 70 °C for 10 min, the
447 samples were placed on ice. Subsequently, 9 µL of a reverse transcription master mix was
448 introduced, with final concentrations of 1x First Strand Buffer, 10 mM DTT, 0.5 mM
449 dNTPs, 1 U/µL RNAse Inhibitor, and 10 U/µL M-MLV transcriptase. The reverse
450 transcription procedure involved annealing for 5 min at 25°C, followed by elongation for
451 60 min at 37°C, which was executed using a Mastercycler Nexus (Eppendorf, Hamburg,
452 Germany). The cDNA was subjected to digestion with 1 U of DNase at 37°C for 15 min,
453 followed by heat inactivation at 75°C for 10 min. The resultant cDNA was then diluted at
454 a 1:5 ratio with nuclease-free water (Ambion, Thermo Fisher Scientific).

455 Quantitative real-time RT-PCR analysis was carried out using the SYBR Green LC480
456 system from Roche Diagnostics. A mixture comprising 2.5 µL of both forward and reverse
457 primer dilutions (0.5 µM each) and 5 µL of LC480 SYBR Green I Master mix (Roche
458 Diagnostics) was prepared per well in a 96-well plate format. Additionally, 2.5 µL of cDNA
459 was added to each well. Each sample was measured in duplicate, and the plates were
460 centrifuged for 2 minutes at 1 000 rpm prior to initiating the measurements using the
461 standard program outlined in Table 4.7 on the Light Cycler 480 II (Roche Diagnostics). The

462 gene expression levels of the various samples were normalized to the housekeeping gene
463 ribosomal protein L19 (RPL19). The relative gene expression was determined using the
464 ΔΔCT method, with the specificity of the primers verified by analyzing the melting curve.

465 **Table 2: List of primers (FW: Forward primer, RV: Reverse Primer)**

Target Gene	**Target Species**		**Sequence 5'-3'**
B-catenin	human	FW	CATCTACACAGTTTGATGCTGCT
		RV	GCAGTTTTGTCAGTTCAGGGA
claudin 2 (CLDN2)	human	FW	ATCGCTCCAACTACTACGATGC
		RV	TGAACTCACTCTTGACTTTGGGA
E-Cadherin (CDH1)	human	FW	ATTTTTCCCTCGACACCCGAT
		RV	TCCCAGGCGTAGACCAAGA
ITGB3	human	FW	CATGAAGGATGATCTGTGGAGC
		RV	AATCCGCAGGTTACTGGTGAG
N-Cadherin (CDH2)	human	FW	AGCCAACCTTAACTGAGGAGT
		RV	GGCAAGTTGATTGGAGGGATG
PSME4	human	FW	ATTTGGAGTTACCCTGGAGACC
		RV	GCAGCTTTTCACGAGTGTTTTG
RPL19	human	FW	TGTACCTGAAGGTGAAGGGG
		RV	GCGTGCTTCCTTGGTCTTAG
Vimentin (VIM)	human	FW	TGCCGTTGAAGCTGCTAACTA

		RV	CCAGAGGGAGTGAATCCAGATTA

466

467 **Bulk mRNA sequencing and analysis**

468 A total of 1.5 million A549 cells and 1 million H1299 cells were cultured in 15 cm dishes and
469 incubated for 48 hours. Total RNA was isolated utilizing the Total RNA kit (Peqlab, VWR).
470 Subsequently, the samples were dispatched to the Core Facility Next-Generation
471 Sequencing at the Helmholtz Center Munich. The RNA integrity number (RIN) was assessed
472 using the Agilent 2100 Bioanalyzer system, and concentration was quantified using the
473 Qubit 2.0 RNA BR assay (Invitrogen). RNAs with RIN values exceeding 6 were chosen for
474 total RNA sequencing (ribo-depleted), a method that effectively detects essential coding
475 and non-coding transcripts by removing highly abundant rRNA species.

476 Library preparation for both human and mouse samples involved using the TruSeq stranded
477 total-RNA Library Preparation kit (Illumina) with 1 µg of RNA, following the kit's protocol.
478 Following a final quality control step, the libraries were subjected to paired-end sequencing
479 (2x150 bases) on the Hiseq 4000 sequencer (Illumina), targeting a depth of at least 40
480 million paired reads per sample. Subsequent to sequencing, initial processing
481 (demultiplexing) of raw data to fastq files was performed using the bcl2fastq v2.20 program
482 from Illumina.

483 For RNA sequencing file alignment, the STAR tool was employed with the GRCh38/hg38
484 version. To estimate transcript abundances, the FeatureCounts function within the
485 Subread2 package was utilized in the Unix environment. Initially, the gene-code ReleaseM23
486 (GRCm38.p6) served as the gene annotation. Subsequently, data underwent filtering,

487 normalization, and differential gene expression analysis using relevant packages within the
488 R programming environment.
489 limma: (https://bioconductor.org/packages/release/bioc/html/limma.html)
490 edgeR: (https://bioconductor.org/packages/release/bioc/html/edgeR.html)

491 **Animal experiments**

492 The experimental procedures involved NOD/SCID mice purchased from Charles River
493 (Freiburg, Germany) (RRID:IMSR_CRL:394) and experiments were performed according to
494 local regulations in Bavaria, Germany (TVA approval number ROB-55.2-2532.Vet_02-20-
495 197). Male and female animals of 6-8 weeks of age were used in the experiments, the
496 sample size was determined beforehand through a G*power analysis. We used G*Power
497 v3.1.9.7. (http://www.gpower.hhu.de/; accessed on 14.10.2020, RRID:SCR_013726) and
498 calculated $\alpha = 0.054$ and $\beta = 0.217$ as acceptable sizes. According to this calculation and to
499 demonstrate an effect size of $f > 0.05$ with $\alpha < 0.05$ and $\beta < 0.20$, we needed at least a
500 sample size of $n = 10$ per group. We therefore used 12 mice per group, taking into account
501 20% reserve animals. Experimental procedures were randomized across different cages. The
502 animals were anaesthetized before being injected with $3x10^6$ PA200 WT or PA200 KO cells in
503 150 µl PBS, and their body weight and tumor size were measured regularly. Mice had to be
504 sacrificed once their tumor burden reached the maximal size, the primary tumor had
505 necrosis or 10 weeks after the cell injection. Once the endpoint conditions were met, the
506 mice were euthanized using lethal anesthesia for organ harvesting and further
507 examinations.

508 **Immunohistochemical analysis of mouse and human tissues**

509 Excised mice tissue specimens were fixed in a 4% (w/v) solution of formalin, followed by
510 paraffin embedding and sectioning into slices measuring 3 µm thick. These sections were

511 subsequently stained using hematoxylin and eosin (HE) staining. The staining procedure was
512 carried out using the HistoCore SPECTRA ST automated slide stainer (Leica, Wetzlar,
513 Germany) with ready-made staining reagents (Histocore Spectra H&E Stain System S1, Leica)
514 following the instructions provided by the manufacturer. Immunohistochemical staining was
515 performed following standardized protocols on a Discovery Ultra automated stainer
516 (Ventana Medical Systems, Tucson, Arizona, USA). Polyclonal rat anti-Ki67 (1:1 000, Abcam)
517 or anti-PSME4 (sc-135512, Santa Cruz, RRID:AB_2171430) was used as a primary antibody.
518 Signal detection was achieved using the Discovery® DAB Map Kit (Ventana Medical Systems,
519 Tucson, AZ). The stained tissue sections were then digitally scanned using an AxioScan.Z1
520 digital slide scanner (Zeiss) equipped with a 20x magnification objective.
521 Human lung tissue obtained from patients surgically treated for lung cancer was provided by
522 the Asklepios Biobank for Lung Disease, Gauting, Germany. Samples were approved with
523 ethical consent obtained from the ethics committee of Ludwig-Maximilians University
524 Munich, in accordance with national and international guidelines (project number 333-10).
525 Paraffin embedded human tissues were cut in 3 µm thick sections using the Hyrax M55
526 microtome (Zeiss). Tissue sections were incubated for one hour at 60 °C in order to melt
527 paraffin, deparaffinized by incubating two times in xylene for 5 min and rehydrated in a
528 descending alcohol series (100 %, 90 %, 80 % and 70 % (v/v)) for 1 min. To block
529 endogenous protease activity and to permeabilize sections for nuclear staining they were
530 incubated in a methanol/hydrogen peroxide (80 %/1.8 % (v/v)) solution for 20 min. Tissue
531 sections were rinsed in Milli-Q® water and heat-induced antigen retrieval was performed in
532 citrate buffer pH 6 using a decloaking chamber (Biocare Medical, Zytomed Berlin, Germany).
533 After washing with TBST unspecific binding sites were blocked for 30 min with Rodent Block
534 M (Biocare Medical). The slides were washed again in TBST and incubated with anti-PA200

535 antibody (sc-135512, Santa Cruz, RRID:AB_2171430) diluted in Antibody Diluent (DAKO) for
536 1 h at RT. After extensive washing in TBST, sections were incubated with MACH 2 Rabbit AP-
537 Polymer (Biocare Medical) for 30 min at RT. Sections were rinsed again in TBST and
538 incubated in Vulcan Fast Red AP substrate solution (Biocare Medical) for 10 min. Tissue
539 sections were washed in TBST and MilliQ® water and hematoxylin counterstaining (Roth)
540 was performed to visualize nuclei. After repeated washing in TBST, sections were
541 dehydrated in ethanol and xylene and mounted using Entellan mounting medium (Merck
542 Millipore, Darmstadt, Germany). Slides were imaged using the MIRAX scanning system
543 (Zeiss). Stainings were analyzed by an expert clinical pathologist blinded to the sample
544 identity. Semiquantitative scores for PA200 expression were obtained by defining the
545 percentage of PA200 positively stained tumor areas multiplied by the intensity of staining as
546 graded between 1 (weak) to 3 (strong). Scores were dichotomized into high (>80) and low
547 (<80) expressing tumors with the score 80 representing the median of all samples and
548 PA200 expression scores were correlated with survival of the patients for this cohort.

549 **Statistical analysis**

550 The specific statistical analyses for each panel are provided in the corresponding figure
551 legends. Statistical significance was denoted in the figures as follows: * for $p < 0.05$, ** for p
552 < 0.01, *** for $p < 0.001$, or **** for $p < 0.0001$. The figures display data as mean ± SEM. All
553 statistical analyses were performed using GraphPad Prism software (version 10,
554 RRID:SCR_002798).

555 **REFERENCES**

556 1 Coux O, Zieba BA, Meiners S. The Proteasome System in Health and Disease. *Advances in*
557 *experimental medicine and biology* 2020; **1233**: 55–100.

558 2 Wang X, Meul T, Meiners S. Exploring the proteasome system: A novel concept of
559 proteasome inhibition and regulation. *Pharmacology & Therapeutics* 2020; : 107526.

560 3 Kammerl IE, Meiners S. Proteasome function shapes innate and adaptive immune
561 responses. *American Journal of Physiology-Lung Cellular and Molecular Physiology* 2016;
562 **311**: L328–L336.

563 4 Bard JAM, Goodall EA, Greene ER, Jonsson E, Dong KC, Martin A. Structure and Function
564 of the 26S Proteasome. *Annual review of biochemistry* 2018; **87**: 697–724.

565 5 Khor B, Bredemeyer AL, Huang CC-Y, Turnbull IR, Evans R, Maggi LB *et al.* Proteasome
566 Activator PA200 Is Required for Normal Spermatogenesis. *Molecular and cellular biology*
567 2006; **26**: 2999–3007.

568 6 Blickwedehl J, Agarwal M, Seong C, Pandita RK, Melendy T, Sung P *et al.* Role for
569 proteasome activator PA200 and postglutamyl proteasome activity in genomic stability.
570 *Proceedings of the National Academy of Sciences of the United States of America* 2008;
571 **105**: 16165–70.

572 7 Blickwedehl J, McEvoy S, Wong I, Kousis P, Clements J, Elliott R *et al.* Proteasomes and
573 Proteasome Activator 200 kDa (PA200) Accumulate on Chromatin in Response to
574 Ionizing Radiation. *Radiation Research* 2007; **167**: 663–674.

575 8 Douida A, Batista F, Robaszkiewicz A, Boto P, Aladdin A, Szenykiv M *et al.* The
576 proteasome activator PA200 regulates expression of genes involved in cell survival upon
577 selective mitochondrial inhibition in neuroblastoma cells. *J Cell Mol Med* 2020; **24**: 6716–
578 6730.

579 9 Welk V, Coux O, Kleene V, Abeza C, Truembach D, Eickelberg O *et al.* Inhibition of
580 Proteasome Activity Induces Formation of Alternative Proteasome Complexes. *Journal of*
581 *Biological Chemistry* 2016; **291**: jbc.M116.717652.

582 10 Welk V, Meul T, Lukas C, Kammerl IE, Mulay SR, Schamberger AC *et al.* Proteasome
583 activator PA200 regulates myofibroblast differentiation. *Scientific Reports* 2019; **9**:
584 15224.

585 11 Lin C, Li H, Liu J, Hu Q, Zhang S, Zhang N *et al.* Arginine hypomethylation-mediated
586 proteasomal degradation of histone H4—an early biomarker of cellular senescence. *Cell*
587 *Death Differ* 2020; **27**: 2697–2709.

588 12 Jiang T-X, Ma S, Han X, Luo Z-Y, Zhu Q-Q, Chiba T *et al.* Proteasome activator PA200
589 maintains stability of histone marks during transcription and aging. *Theranostics* 2021;
590 **11**: 1458–1472.

591 13 VerPlank JJ, Gawron JM, Silvestri NJ, Wrabetz L, Feltri ML. Knockout of PA200 improves
592 proteasomal degradation and myelination in a proteotoxic neuropathy. *Life Sci Alliance*
593 2024; **7**: e202302349.

594 14 Aladdin A, Yao Y, Yang C, Kahlert G, Ghani M, Király N *et al.* The Proteasome Activators
595 Blm10/PA200 Enhance the Proteasomal Degradation of N-Terminal Huntingtin.
596 *Biomolecules* 2020; **10**: 1581.

597 15 Javitt A, Shmueli MD, Kramer MP, Kolodziejczyk AA, Cohen IJ, Radomir L *et al.* The
598 proteasome regulator PSME4 modulates proteasome activity and antigen diversity to
599 abrogate antitumor immunity in NSCLC. *Nat Cancer* 2023; **4**: 629–647.

600 16 Yu Z, Wei X, Liu L, Sun H, Fang T, Wang L *et al.* Indirubin-3'-monoxime acts as
601 proteasome inhibitor: Therapeutic application in multiple myeloma. *eBioMedicine* 2022;
602 **78**: 103950.

603 17 Yazgili AS, Ebstein F, Meiners S. The Proteasome Activator PA200/PSME4: An Emerging
604 New Player in Health and Disease. *Biomolecules* 2022; **12**: 1150.

605 18 Bölükbas DA, Datz S, Meyer-Schwickerath C, Morrone C, Doryab A, Gößl D *et al.*
606 Organ-Restricted Vascular Delivery of Nanoparticles for Lung Cancer Therapy. *Advanced*
607 *Therapeutics* 2020; **3**: 2000017.

608 19 Toste Rêgo A, da Fonseca PCA. Characterization of Fully Recombinant Human 20S and
609 20S-PA200 Proteasome Complexes. *Molecular Cell* 2019; **76**: 138-147.e5.

610 20 Yazgili AS, Meul T, Welk V, Semren N, Kammerl IE, Meiners S. In-gel proteasome assay to
611 determine the activity, amount, and composition of proteasome complexes
612 from mammalian cells or tissues. *STAR Protoc* 2021; **2**: 100526.

613 21 Hanahan D, Weinberg R a. Hallmarks of cancer: the next generation. *Cell* 2011; **144**: 646–
614 74.

615 22 Qian M-X, Pang Y, Liu CH, Haratake K, Du B-Y, Ji D-Y *et al.* Acetylation-Mediated
616 Proteasomal Degradation of Core Histones during DNA Repair and Spermatogenesis. *Cell*
617 2013; **153**: 1012–1024.

618 23 Mandemaker IK, Geijer ME, Kik I, Bezstarosti K, Rijkers E, Raams A *et al.* DNA
619 damage-induced replication stress results in PA200-proteasome-mediated degradation
620 of acetylated histones. *EMBO reports* 2018; : e45566.

621 24 Kefala Stavridi A, Gontier A, Morin V, Frit P, Ropars V, Barboule N *et al.* Structural and
622 functional basis of inositol hexaphosphate stimulation of NHEJ through stabilization of
623 Ku-XLF interaction. *Nucleic Acids Research* 2023; **51**: 11732–11747.

624 25 Guan H, Wang Y, Yu T, Huang Y, Li M, Saeed AFUH *et al.* Cryo-EM structures of the
625 human PA200 and PA200-20S complex reveal regulation of proteasome gate opening
626 and two PA200 apertures. *PLoS Biol* 2020; **18**: e3000654.

627 26 Sundararajan R, Salameh T, Camarillo IG, Prabu RR, Natarajan A, Sankaranarayanan K.
628 Irreversible electroporation: a drug-free cancer treatment. In: *Electroporation-Based*
629 *Therapies for Cancer*. Elsevier, 2014, pp 219–243.

630 27 Tripathi SC, Peters HL, Taguchi A, Katayama H, Wang H, Momin A *et al.*
631 Immunoproteasome deficiency is a feature of non-small cell lung cancer with a
632 mesenchymal phenotype and is associated with a poor outcome. *Proceedings of the*
633 *National Academy of Sciences* 2016; : 201521812.

634 28 Blickwedehl J, Olejniczak S, Cummings R, Sarvaiya N, Mantilla A, Chanan-Khan A *et al.*
635 The Proteasome Activator PA200 Regulates Tumor Cell Responsiveness to Glutamine
636 and Resistance to Ionizing Radiation. *Mol Cancer Res* 2012; **10**: 937–944.

637 29 Parvani JG, Gujrati MD, Mack MA, Schiemann WP, Lu Z-R. Silencing β3 Integrin by
638 Targeted ECO/siRNA Nanoparticles Inhibits EMT and Metastasis of Triple-Negative
639 Breast Cancer. *Cancer Research* 2015; **75**: 2316–2325.

640 30 Cheng C, Liu D, Liu Z, Li M, Wang Y, Sun B *et al.* Positive feedback regulation of lncRNA
641 TPT1-AS1 and ITGB3 promotes cell growth and metastasis in pancreatic cancer. *Cancer*
642 *Science* 2022; **113**: 2986–3001.

643 31 Zepp JA, Morley MP, Loebel C, Kremp MM, Chaudhry FN, Basil MC *et al.* Genomic,
644 epigenomic, and biophysical cues controlling the emergence of the lung alveolus. *Science*
645 2021; **371**: eabc3172.

646 32 Lei Y, Huang K, Gao C, Lau QC, Pan H, Xie K *et al.* Proteomics Identification of ITGB3 as a
647 Key Regulator in Reactive Oxygen Species-induced Migration and Invasion of Colorectal
648 Cancer Cells. *Molecular & Cellular Proteomics* 2011; **10**: M110.005397.

649 33 Meul T, Berschneider K, Schmitt S, Mayr CH, Mattner LF, Schiller HB *et al.* Mitochondrial
650 Regulation of the 26S Proteasome. *Cell reports* 2020; **32**: 108059.

651 34 Sullivan LB, Gui DY, Hosios AM, Bush LN, Freinkman E, Vander Heiden MG. Supporting
652 Aspartate Biosynthesis Is an Essential Function of Respiration in Proliferating Cells. *Cell*
653 2015; **162**: 552–563.

654 35 Franken NAP, Rodermond HM, Stap J, Haveman J, Van Bree C. Clonogenic assay of cells
655 in vitro. *Nat Protoc* 2006; **1**: 2315–2319.

656 36 Carpentier G, Berndt S, Ferratge S, Rasband W, Cuendet M, Uzan G *et al.* Angiogenesis
657 Analyzer for ImageJ — A comparative morphometric analysis of "Endothelial Tube
658 Formation Assay" and "Fibrin Bead Assay". *Sci Rep* 2020; **10**: 11568.

659 37 Burgstaller G, Oehrle B, Koch I, Lindner M, Eickelberg O. Multiplex profiling of cellular
660 invasion in 3D cell culture models. *PloS one* 2013; **8**: e63121.

661

662

663 **ACKNOWLEDGEMENT**

664 This work was supported by the Leibniz Association granted to SM. We are grateful for the
665 technical support of Core Facility Genomics at Helmholtz Zentrum München. We also like to
666 thank Elvira Stacher-Priehse from the Askepios Klinik Gauting for her analysis of the
667 histological stainings.

668

669 **CONFLICT OF INTEREST STATEMENT**

670 The authors declare that there is no conflict of interest.

671

672 **AUTHOR CONTRIBUTION STATEMENT**

673 ASY, FK, LZ, GGG, SJB, VW, TM performed experiments; ASY, LZ, GGG, SJB, TG, GTS, VW and
674 NR analyzed the data; ASY, SM wrote and revised the manuscript; SM developed and
675 coordinated the project.

676

677 **ETHICS STATEMENT**

678 Animal experiments were performed according to local regulations in Bavaria, Germany
679 (TVA approval number ROB-55.2-2532.Vet_02-20-197). The maximal tumor size permitted
680 by the ethics committee was 20 mm. Once the tumor size approached this volume, mice
681 were sacrificed. Human lung tissue obtained from patients surgically treated for lung cancer
682 was provided by the Asklepios Biobank for Lung Disease, Gauting, Germany. Samples were
683 approved with ethical consent obtained from the ethics committee of Ludwig-Maximilians
684 University Munich, in accordance with national and international guidelines such as the
685 Declaration of Helsinki (project number 333-10).

686

FUNDING STATEMENT

The study was supported by a BMBF grant to SM and GTS (16GW0287) and a DFG/ANR grant to SM (ME2002/6-1).

DATA AVAILABILITY

The data generated in this study have been made publicly available in Gene Expression Omnibus under GSE288117 (GEO, RRID:SCR_005012).

696 **FIGURE LEGENDS**

697

698 **Figure 1: Deletion of PA200 in lung cell lines differentially impacts proteasome activity.**
699 PA200 KO was generated by CRISPR/Cas9 in A549 and H1299 cell lines. **A)** Relative PA200
700 mRNA expression was determined in A549 and H1299 WT and KO cell lines by RTqPCR using
701 RPL19 as a housekeeping mRNA ($2^{-deltaCT}$ method, ****$p < 0.0001$, ordinary 2-way ANOVA for
702 analysis of WT vs KO and unpaired t test for A549 and H1299 comparison, n=3 clones). **B)**
703 Representative images and relative protein expression levels as determined by Western
704 blotting. β-actin served as a housekeeping protein to ensure equal protein loading. Total
705 proteasome activity of CT-L, T-L and C-L was analyzed in the different clones of **C)** A549 and
706 **D)** H1299 (normalized to the respective WT control clones).

707

708 **Figure 2: PA200 KO differentially affects proteasome composition and activity in lung**
709 **cancer cell lines.** The composition and activity of proteasome complexes was compared
710 between the selected WTs and KO cell lines. The gels were blotted after the in-gel
711 proteasome CT-L activity of native gels to determine the distribution of catalytic subunits
712 and activators subunits in proteasome complexes of **(A)** A549 cells and **(B)** NCI-H1299 cells.
713 Quantifications are shown below the respective images. (*$p < 0.05$, **$p < 0.01$, ***$p < 0.001$,
714 ordinary two-way ANOVA with Šídák test, n=3, different passages).

715

716 **Figure 3: Deletion of PA200 in lung cancer cell lines does not consistently alter tumor cell**
717 **growth. A)** Pools of three A549 and H1299 WT and KO cell clones were seeded and counted
718 on different days to track the doubling time. Data were normalized to the respective WT
719 control (n=3, different passages, unpaired t-test). **B)** A clonogenic assay optimized for A549

720 and H1299 pools of clones. Visible colonies that had at least 50 cells were counted and
721 quantified (n=3, different passages, unpaired t-test). Primary tumor volumes of **C)** A549 and
722 **D)** H1299 cells were monitored over time (ordinary 2-way ANOVA, WT cells injected into 10
723 mice and PA200 KO cells injected into 15 mice, *$p < 0.05$, ***$p < 0.001$). Ki67 staining of
724 dissected primary tumors from **E)** A549 and **F)** H1299 WT and respective KO cells (unpaired
725 t-test).
726
727 **Figure 4: Deletion of PA200 regulates invasion and migration capacity of lung cancer cells.**
728 **A)** An 3D invasion assay was employed for A549 WT and KO cell pools to determine their
729 invasive capacity. Representative images of the spheroids after 72 h of initial seeding and 72
730 h after embedding in the Collagen G+Matrigel membrane (left panel). The invasion
731 percentage was calculated by comparing the 72h and 144 h area differences (right panel,
732 n=3, different passages). **B)** Representative images of the Boyden chamber migration assay
733 of the H1299 cells (left panel) and quantifications (right panel) are shown (n=3, different
734 passage, two-tailed unpaired t-test). Representative photos of the wound closures of **(C)**
735 A549 and **(D)** H1299 WT and KO cells were taken every 12 h up to 48 h and quantified (right
736 panel, ordinary 2way ANOVA, n=3, different passages). **E)** Protein levels of epithelial and
737 mesenchymal markers were quantified (right panel, n=3, different passages, 2-way ANOVA)
738 in A549 and H1299 WT and KO pools and β-actin (representative image) served as protein
739 loading control. For quantification, relative expression levels were normalized to the
740 respective WT controls of each cell line. *$p < 0.05$, **$p < 0.01$, ***$p < 0.001$, ****$p < 0.0001$.
741
742 **Figure 5: RNA sequencing analysis reveals differential transcriptome regulation upon**
743 **PA200 deletion in lung cancer cell lines.** The effects of PA200 deficiency in A549 and H1299

744 on transcriptional regulation were analyzed by RNA sequencing. The results were filtered,
745 and differentially expressed genes (DEGs) (|FC| ≥ 1, p ≤ 0.05, FDR ≤ 0.05) were plotted in
746 volcano plots for **A)** A549 and **B)** H1299 cell lines. **C)** Venn diagram of the co-regulated and
747 counter-regulated DEGs showed transcriptomic differences between the two lines. Bubble
748 charts of Reactome analysis showed the significantly up (left panel) or down (right panel)
749 regulated pathways in **D-E)** A549 and **F-G)** H1299 cells. (n=3, WT and KO).
750
751 **Figure 6: Differential interactome of PA200 in lung cancer cell lines.** Interactors of PA200
752 were captured by PA200 immunoprecipitation and analyzed by mass spectrometry. PA200
753 KO cell lines were used as control lysates. **A)** Representative images of the Western blot
754 analysis of the PA200 immunoprecipitation with A549 and H1299 cell lysates, with α1-7 and
755 PA200 antibodies. **B)** Venn diagram showing the significantly enriched proteins in pulldowns
756 of PA200 (PSME4) in A549 and H1299 cell lines. Volcanoplot showing all significantly
757 enriched interacting proteins of PA200 compared to control lysates for **C)** A549 and **D)**
758 H1299 cells in light pink circles (FC ≥ 1.5, p ≤ 0.05). The PA200 interactors were analyzed with
759 EnrichR to highlight the molecular signature (MsigDB) differences of **E)** A549 and **F)** H1299
760 PA200 interactomes. LC-MS/MS was performed by Dr J. Merl-Pham, Research Unit Protein
761 Science and Metabolomics and Proteomics Core Facility (HMGU, n=3 different passages).
762
763

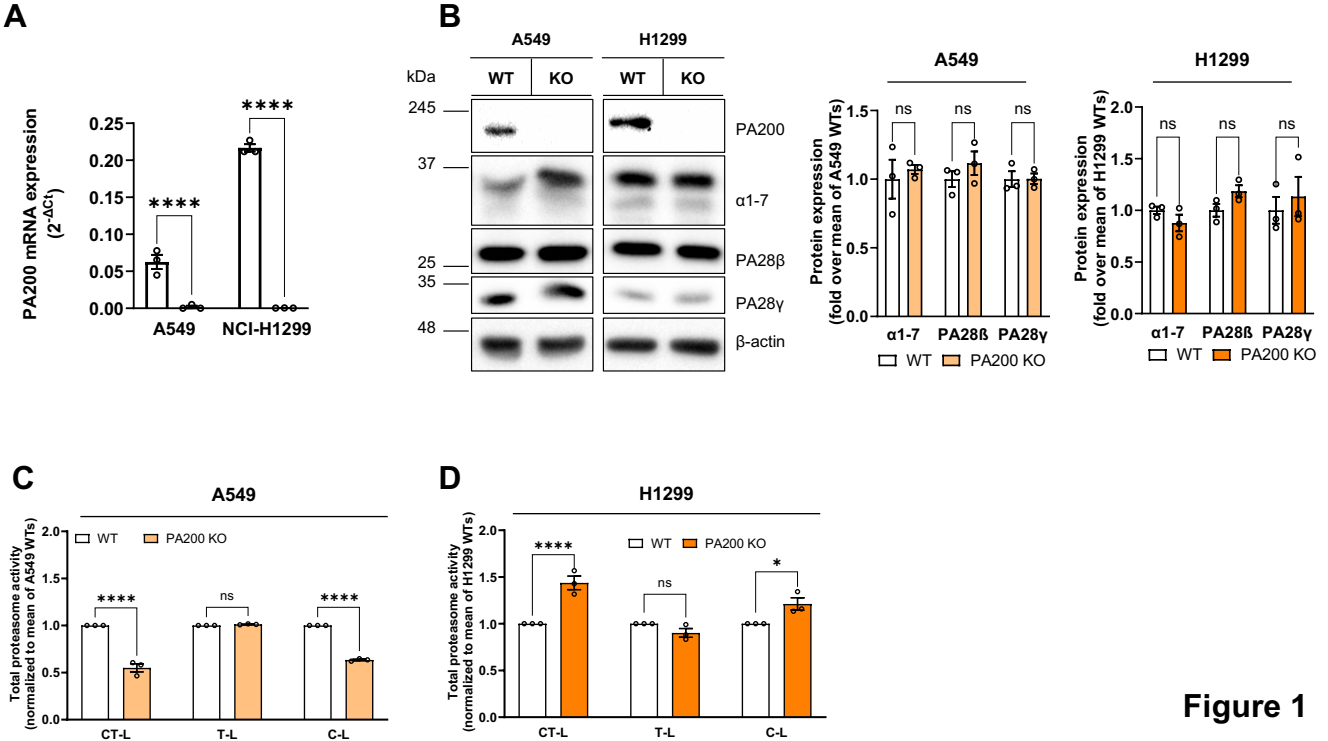
A
PA200 mRNA expression
(2^-ΔCt)
0.25
0.20
0.15
0.10
0.05
0.00
****
****
A549
NCI-H1299
B
A549
H1299
kDa
WT
KO
WT
KO
245
37
25
35
48
PA200
α1-7
PA28β
PA28γ
β-actin
A549
Protein expression
(fold over mean of A549 WTs)
ns
α1-7
PA28ß
PA28γ
WT
PA200 KO
H1299
Protein expression
(fold over mean of H1299 WTs)
C
A549
Total proteasome activity
(normalized to mean of A549 WTs)
WT
PA200 KO
****
ns
****
CT-L
T-L
C-L
D
H1299
Total proteasome activity
(normalized to mean of H1299 WTs)
****
ns
*
CT-L
T-L
C-L

Figure 1

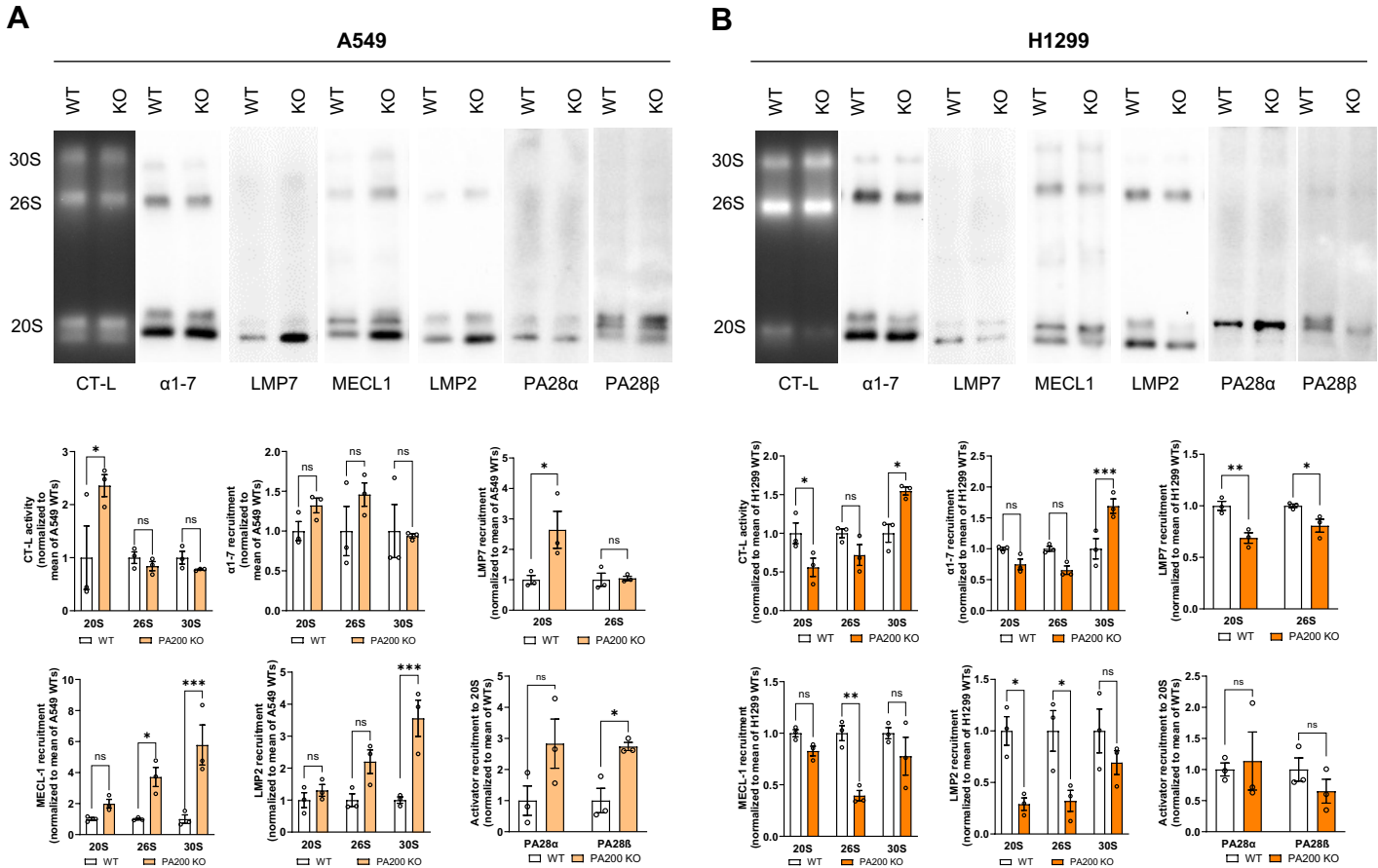
A
A549
WT
KO
30S
26S
20S
CT-L
α1-7
LMP7
MECL1
LMP2
PA28α
PA28β
CT-L activity (normalized to mean of A549 WTs)
α1-7 recruitment (normalized to mean of A549 WTs)
LMP7 recruitment (normalized to mean of A549 WTs)
MECL-1 recruitment (normalized to mean of A549 WTs)
LMP2 recruitment (normalized to mean of A549 WTs)
Activator recruitment to 20S (normalized to mean of WTs)
20S
26S
30S
PA28α
PA28ß
WT
PA200 KO
B
H1299
CT-L activity (normalized to mean of H1299 WTs)
α1-7 recruitment (normalized to mean of H1299 WTs)
LMP7 recruitment (normalized to mean of H1299 WTs)
MECL-1 recruitment (normalized to mean of H1299 WTs)
LMP2 recruitment (normalized to mean of H1299 WTs)
Activator recruitment to 20S (normalized to mean of WTs)

Figure 2

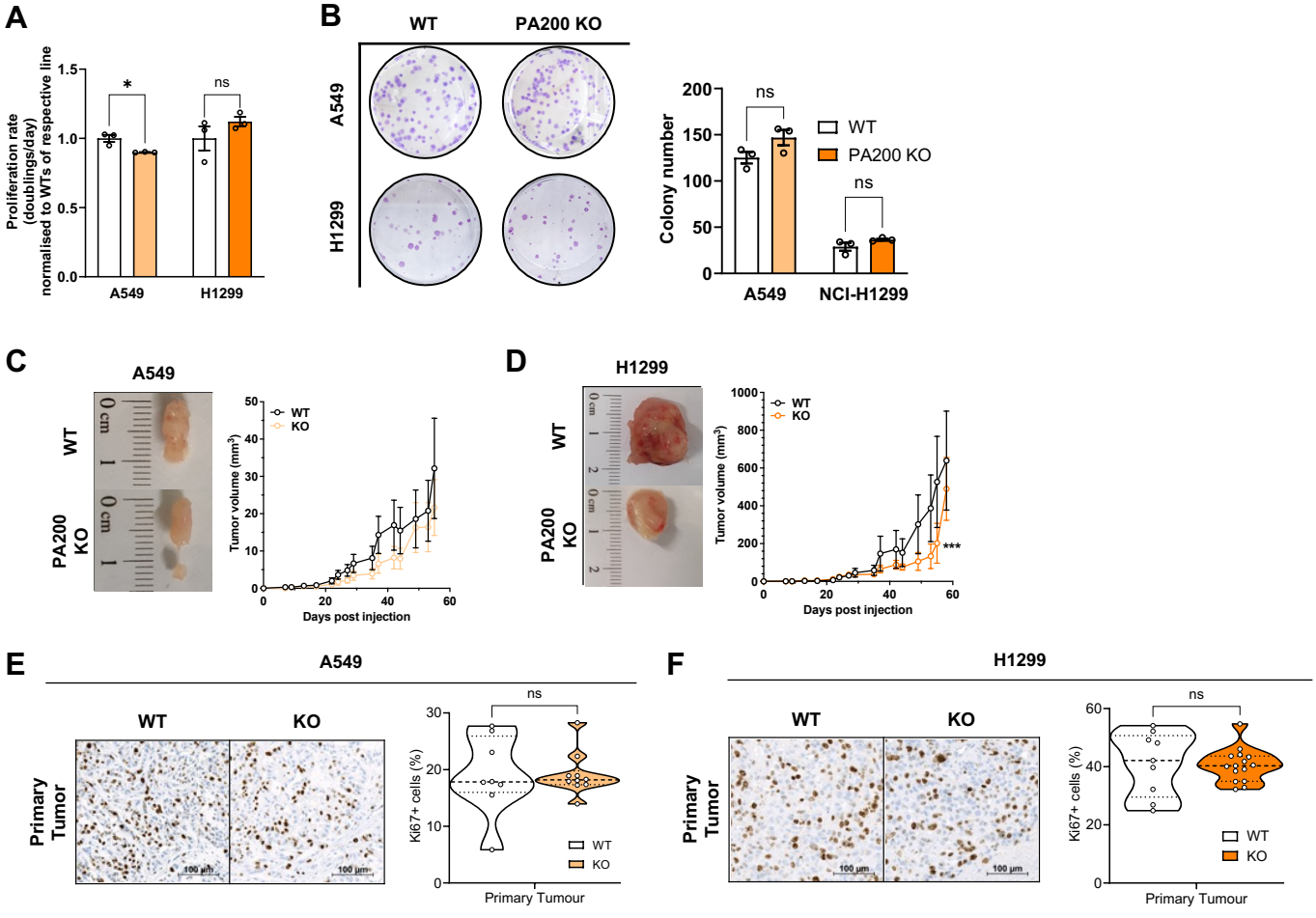
A
Proliferation rate (doublings/day) normalised to WTs of respective line
1.5
1.0
0.5
0.0
*
ns
A549
H1299
B
WT
PA200 KO
A549
H1299
Colony number
200
150
100
50
0
ns
ns
WT
PA200 KO
A549
NCI-H1299
C
A549
WT
PA200 KO
Tumor volume (mm³)
Days post injection
WT
KO
D
H1299
WT
PA200 KO
Tumor volume (mm³)
Days post injection
WT
KO
***
E
A549
WT
KO
Primary Tumor
100 µm
Ki67+ cells (%)
ns
WT
KO
Primary Tumour
F
H1299
WT
KO
Primary Tumor
100 µm
Ki67+ cells (%)
ns
WT
KO
Primary Tumour

Figure 3

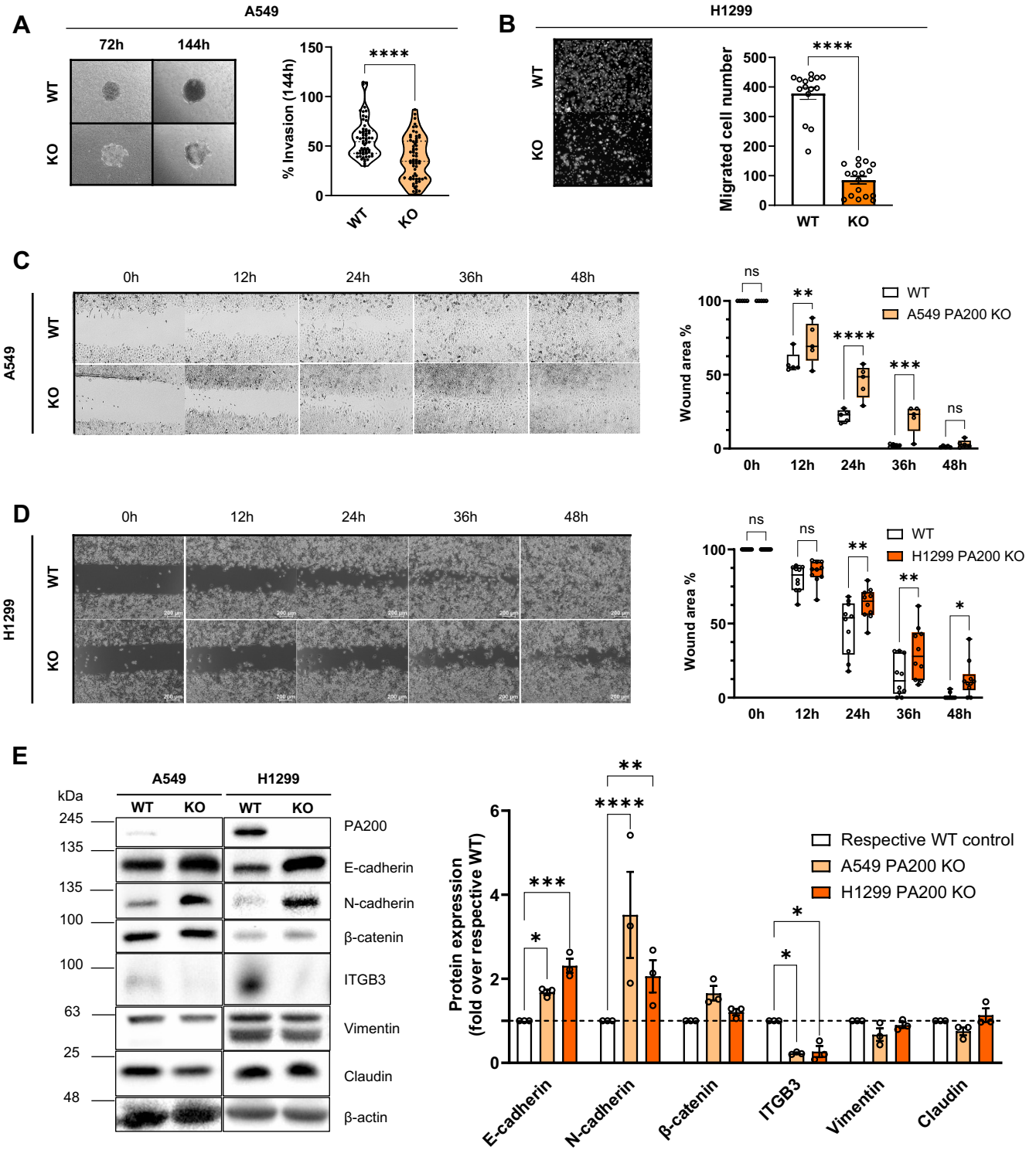
A
A549
72h
144h
WT
KO
% Invasion (144h)
150
100
50
0
****
WT
KO
B
H1299
WT
KO
Migrated cell number
500
400
300
200
100
0
****
WT
KO
C
0h
12h
24h
36h
48h
A549
WT
KO
Wound area %
100
50
0
ns
**
****
***
ns
WT
A549 PA200 KO
0h
12h
24h
36h
48h
D
0h
12h
24h
36h
48h
H1299
WT
KO
Wound area %
100
50
0
ns
ns
**
**
*
WT
H1299 PA200 KO
0h
12h
24h
36h
48h
E
A549
H1299
kDa
WT
KO
WT
KO
245
135
135
100
100
63
25
48
PA200
E-cadherin
N-cadherin
β-catenin
ITGB3
Vimentin
Claudin
β-actin
Protein expression
(fold over respective WT)
6
4
2
0
**
****
***
*
*
*
Respective WT control
A549 PA200 KO
H1299 PA200 KO
E-cadherin
N-cadherin
β-catenin
ITGB3
Vimentin
Claudin

Figure 4

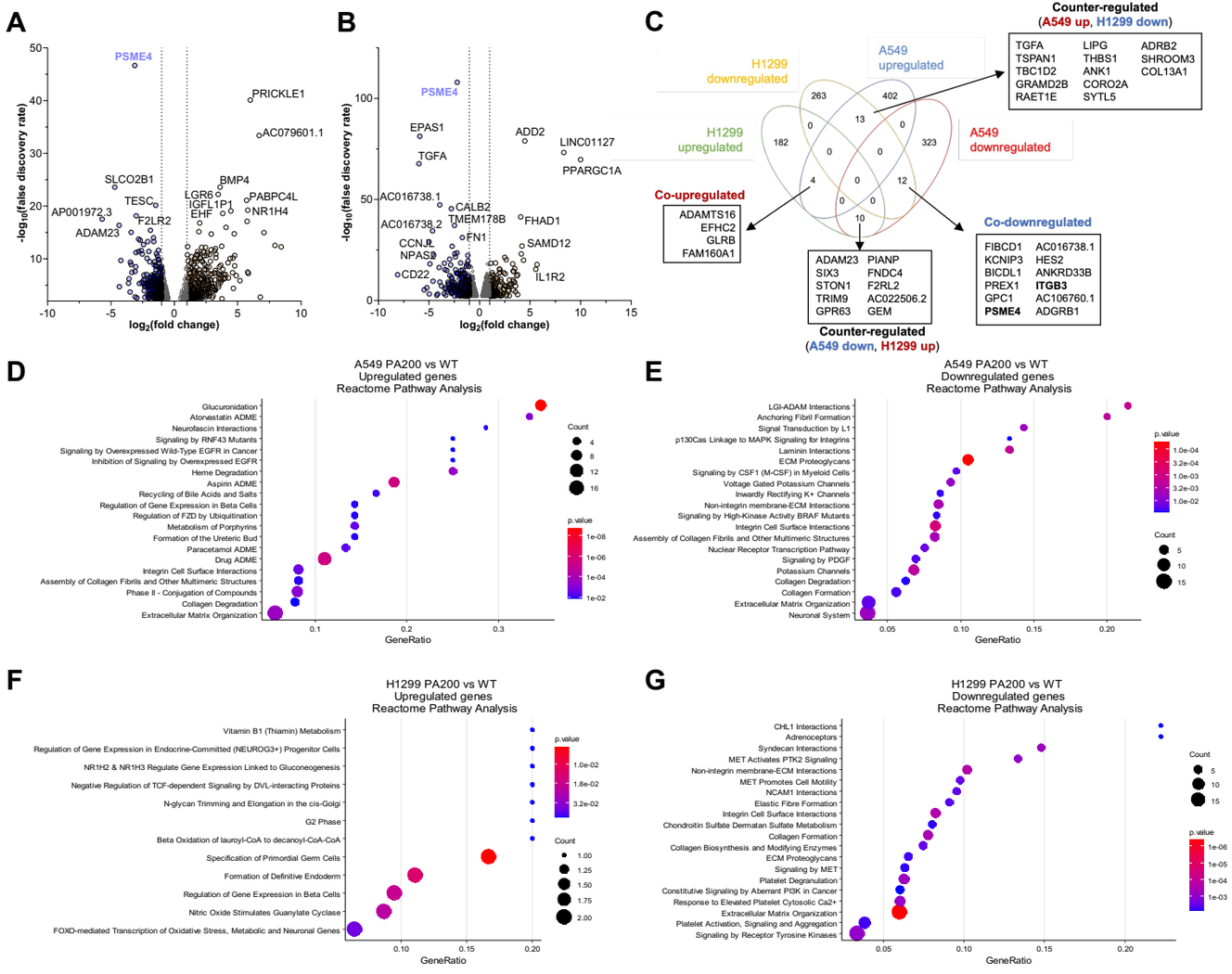
A
PSME4
PRICKLE1
AC079601.1
SLCO2B1
BMP4
TESC
LGR6
IGFL1P1
PABPC4L
AP001972.3
EHF
NR1H4
F2LR2
ADAM23
-log10(false discovery rate)
log2(fold change)
B
PSME4
EPAS1
TGFA
ADD2
LINC01127
PPARGC1A
AC016738.1
CALB2
AC016738.2
TMEM178B
FHAD1
FN1
CCN1
SAMD12
NPAS2
CD22
IL1R2
C
H1299 downregulated
A549 upregulated
H1299 upregulated
A549 downregulated
Counter-regulated (A549 up, H1299 down)
TGFA LIPG ADRB2
TSPAN1 THBS1 SHROOM3
TBC1D2 ANK1 COL13A1
GRAMD2B CORO2A
RAET1E SYTL5
Co-upregulated
ADAMTS16
EFHC2
GLRB
FAM160A1
Co-downregulated
FIBCD1 AC016738.1
KCNIP3 HES2
BICDL1 ANKRD33B
PREX1 ITGB3
GPC1 AC106760.1
PSME4 ADGRB1
ADAM23 PIANP
SIX3 FNDC4
STON1 F2RL2
TRIM9 AC022506.2
GPR63 GEM
Counter-regulated (A549 down, H1299 up)
D
A549 PA200 vs WT
Upregulated genes
Reactome Pathway Analysis
Glucuronidation
Atorvastatin ADME
Neurofascin Interactions
Signaling by RNF43 Mutants
Signaling by Overexpressed Wild-Type EGFR in Cancer
Inhibition of Signaling by Overexpressed EGFR
Heme Degradation
Aspirin ADME
Recycling of Bile Acids and Salts
Regulation of Gene Expression in Beta Cells
Regulation of FZD by Ubiquitination
Metabolism of Porphyrins
Formation of the Ureteric Bud
Paracetamol ADME
Drug ADME
Integrin Cell Surface Interactions
Assembly of Collagen Fibrils and Other Multimeric Structures
Phase II - Conjugation of Compounds
Collagen Degradation
Extracellular Matrix Organization
GeneRatio
Count
p.value
E
A549 PA200 vs WT
Downregulated genes
Reactome Pathway Analysis
LGI-ADAM Interactions
Anchoring Fibril Formation
Signal Transduction by L1
p130Cas Linkage to MAPK Signaling for Integrins
Laminin Interactions
ECM Proteoglycans
Signaling by CSF1 (M-CSF) in Myeloid Cells
Voltage Gated Potassium Channels
Inwardly Rectifying K+ Channels
Non-integrin membrane-ECM Interactions
Signaling by High-Kinase Activity BRAF Mutants
Integrin Cell Surface Interactions
Assembly of Collagen Fibrils and Other Multimeric Structures
Nuclear Receptor Transcription Pathway
Signaling by PDGF
Potassium Channels
Collagen Degradation
Collagen Formation
Extracellular Matrix Organization
Neuronal System
GeneRatio
p.value
Count
F
H1299 PA200 vs WT
Upregulated genes
Reactome Pathway Analysis
Vitamin B1 (Thiamin) Metabolism
Regulation of Gene Expression in Endocrine-Committed (NEUROG3+) Progenitor Cells
NR1H2 & NR1H3 Regulate Gene Expression Linked to Gluconeogenesis
Negative Regulation of TCF-dependent Signaling by DVL-interacting Proteins
N-glycan Trimming and Elongation in the cis-Golgi
G2 Phase
Beta Oxidation of lauroyl-CoA to decanoyl-CoA-CoA
Specification of Primordial Germ Cells
Formation of Definitive Endoderm
Regulation of Gene Expression in Beta Cells
Nitric Oxide Stimulates Guanylate Cyclase
FOXO-mediated Transcription of Oxidative Stress, Metabolic and Neuronal Genes
GeneRatio
p.value
Count
G
H1299 PA200 vs WT
Downregulated genes
Reactome Pathway Analysis
CHL1 Interactions
Adrenoceptors
Syndecan Interactions
MET Activates PTK2 Signaling
Non-integrin membrane-ECM Interactions
MET Promotes Cell Motility
NCAM1 Interactions
Elastic Fibre Formation
Integrin Cell Surface Interactions
Chondroitin Sulfate Dermatan Sulfate Metabolism
Collagen Formation
Collagen Biosynthesis and Modifying Enzymes
ECM Proteoglycans
Signaling by MET
Platelet Degranulation
Constitutive Signaling by Aberrant PI3K in Cancer
Response to Elevated Platelet Cytosolic Ca2+
Extracellular Matrix Organization
Platelet Activation, Signaling and Aggregation
Signaling by Receptor Tyrosine Kinases
GeneRatio
Count
p.value

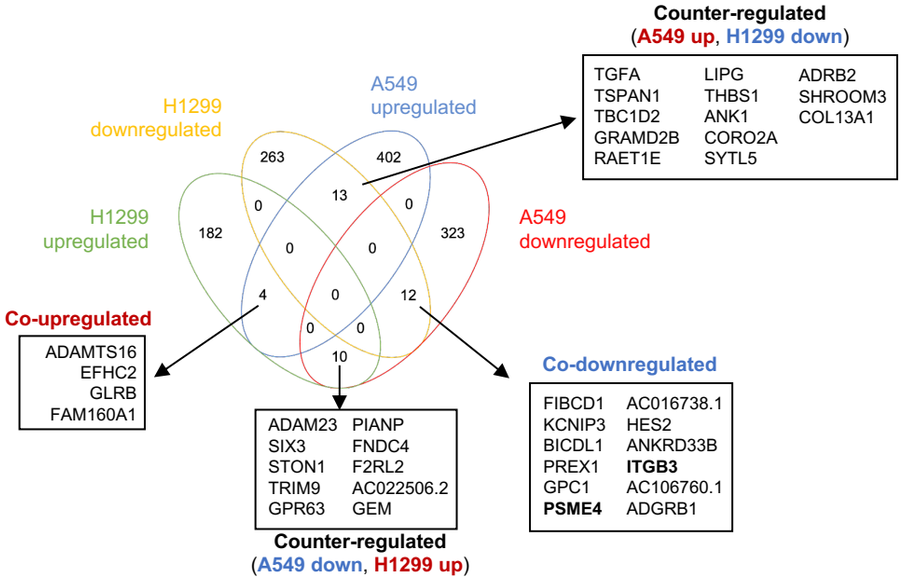
Counter-regulated (A549 up, H1299 down)
TGFA LIPG ADRB2
TSPAN1 THBS1 SHROOM3
TBC1D2 ANK1 COL13A1
GRAMD2B CORO2A
RAET1E SYTL5
H1299 downregulated
A549 upregulated
H1299 upregulated
A549 downregulated
263
402
13
0
182
323
4
12
10
Co-upregulated
ADAMTS16
EFHC2
GLRB
FAM160A1
Co-downregulated
FIBCD1 AC016738.1
KCNIP3 HES2
BICDL1 ANKRD33B
PREX1 ITGB3
GPC1 AC106760.1
PSME4 ADGRB1
ADAM23 PIANP
SIX3 FNDC4
STON1 F2RL2
TRIM9 AC022506.2
GPR63 GEM
Counter-regulated (A549 down, H1299 up)

Figure 5

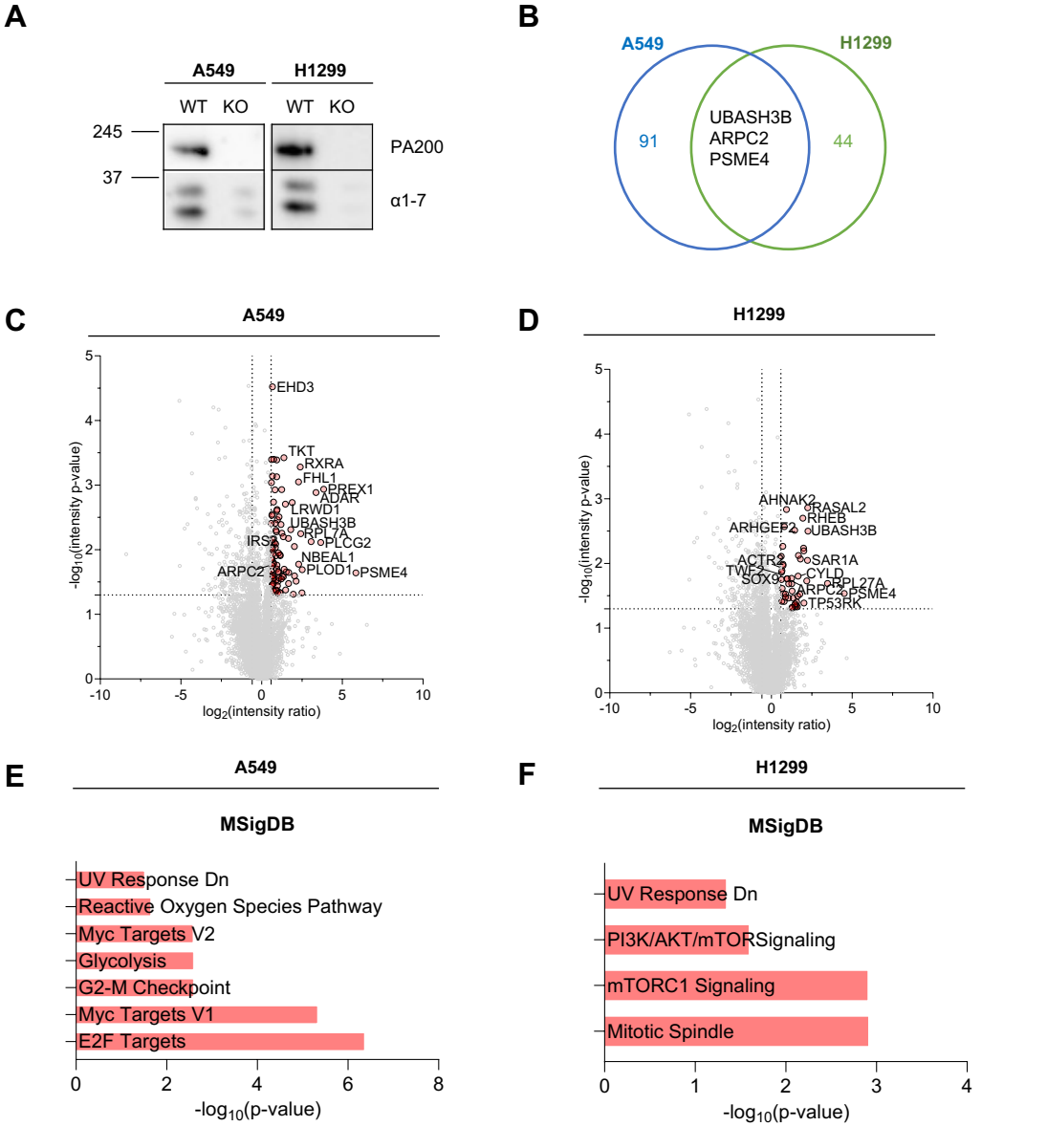
A
A549
H1299
WT KO
WT KO
245
37
PA200
α1-7
B
A549
H1299
91
UBASH3B
ARPC2
PSME4
44
C
A549
EHD3
TKT
RXRA
FHL1
PREX1
ADAR
LRWD1
UBASH3B
RPL7A
PLCG2
IRS2
NBEAL1
ARPC2
PLOD1
PSME4
-log10(intensity p-value)
log2(intensity ratio)
D
H1299
AHNAK2
RASAL2
RHEB
ARHGEF2
UBASH3B
ACTR2
SAR1A
TWF2
CYLD
SOX9
RPL27A
ARPC2
PSME4
TP53RK
-log10(intensity p-value)
log2(intensity ratio)
E
A549
MSigDB
UV Response Dn
Reactive Oxygen Species Pathway
Myc Targets V2
Glycolysis
G2-M Checkpoint
Myc Targets V1
E2F Targets
-log10(p-value)
F
H1299
MSigDB
UV Response Dn
PI3K/AKT/mTORSignaling
mTORC1 Signaling
Mitotic Spindle
-log10(p-value)

Figure 6